JOURNAL OF GEOPHYSICAL RESEARCH, VOL. 109, C06013, doi:10.1029/2003JC002164, 2004

A temperature-dependent, structural-optical model of first-year sea ice

B. Light,[1] G. A. Maykut, and T. C. Grenfell

Department of Atmospheric Sciences, University of Washington, Seattle, Washington, USA

Received 14 October 2003; revised 23 February 2004; accepted 31 March 2004; published 10 June 2004.

[1] A model has been developed that relates the structural properties of first-year sea ice to its inherent optical properties, quantities needed by detailed radiative transfer models. The structural-optical model makes it possible to calculate absorption coefficients, scattering coefficients, and phase functions for the ice from information about its physical properties. The model takes into account scattering by brine inclusions in the ice, gas bubbles in both brine and ice, and precipitated salt crystals. The model was developed using concurrent laboratory measurements of the microstructure and apparent optical properties of first-year, interior sea ice between temperatures of −33°C and −1°C. Results show that the structural-optical properties of sea ice can be divided into three distinct thermal regimes: cold ($T < -23°C$), moderate ($-23°C < T < -8°C$), and warm ($T > -8°C$). Relationships between structural and optical properties in each regime involve different sets of physical processes, of which most are strongly tied to freezing equilibrium of the brine and ice. Volume scattering in cold ice is dominated by the size and number distribution of precipitated hydrohalite crystals. Scattering at intermediate temperatures is controlled by changes in the distribution of brine inclusions, gas bubbles, and mirabilite crystals. Total volume scattering in this regime is approximately independent of temperature because of a balance between increasing and decreasing scattering related to the thermal evolution of these inclusions and scattering by drained inclusions. In warm ice, scattering is controlled principally by temperature-dependent changes in the real refractive index of brine and by the escape of gas bubbles from the ice. Model predictions indicate that scattering coefficients can exceed 3000 m^{-1} for cold ice, averaging ∼450 m^{-1} for moderate and warm ice and reaching a minimum of ∼340 m^{-1} at −8°C. Scattering in all three regimes is very strongly forward peaked, with values of the asymmetry parameter g generally falling between 0.975 ($T = -8°C$) and 0.995 ($T = -33°C$).

INDEX TERMS: 4540 Oceanography: Physical: Ice mechanics and air/sea/ice exchange processes; 4552 Oceanography: Physical: Ocean optics; 4207 Oceanography: General: Arctic and Antarctic oceanography; *KEYWORDS:* radiative transfer, Arctic sea ice, sea ice scattering

Citation: Light, B., G. A. Maykut, and T. C. Grenfell (2004), A temperature-dependent, structural-optical model of first-year sea ice, *J. Geophys. Res.*, *109*, C06013, doi:10.1029/2003JC002164.

1. Introduction

[2] Sea ice is a key element in the Earth's climate system. During the summer, interactions of solar radiation with the sea ice cover and upper ocean contribute to a variety of climatically important processes that control the heat and mass balance of the ice pack. Of particular interest are the effects of this radiation on melting at the top and bottom of the ice, lateral melting on floe edges, the development and evolution of melt ponds, internal heat storage within the ice, heating of the ocean mixed layer, and biological processes within and beneath the ice. These are all elements in a positive feedback between solar radiation, ice extent, and climate. This so-called ice-albedo feedback process is an important topic of current experimental and theoretical research [e.g., *Ebert and Curry*, 1993; *Moritz and Perovich*, 1996; *Holland et al.*, 1997], but details of the numerous physical processes involved in this feedback and their interactions with the ice, ocean, and atmosphere are not yet well understood.

[3] Empirical studies of interactions between shortwave radiation and sea ice have generally included measurements of apparent optical properties as a function of ice type and/or season. *Langleben* [1969, 1971], for example, documented changes in total albedo during the melting and disintegration of nearshore, first-year sea ice. *Grenfell and Maykut* [1977] reported spectral albedos for melting white ice, blue ice, and melt ponds on first-year and multiyear ice. Other work has focused on the temporal evolution of the albedo during the summer melt season [e.g., *Grenfell and Perovich*, 1984; *Perovich*, 1994; *Perovich et al.*, 2002]. Data have also been collected on changes in transmissivity and in-ice

---

[1] Now at Applied Physics Laboratory, Polar Science Center, University of Washington, Seattle, Washington, USA.

0148-0227/04/2003JC002164$09.00

radiance during the melt season [e.g., *Untersteiner*, 1961; *Chernigovskiy*, 1966; *Maykut and Grenfell*, 1975; *Grenfell and Maykut*, 1977; *Mobley et al.*, 1998; *Perovich et al.*, 1998a, 1998b; *Pegau and Zaneveld*, 2000].

[4] The observations indicate that bulk optical properties can be correlated with certain physical properties of the ice, specifically ice temperature, thickness, salinity, and surface conditions. However, we do not yet have sufficient understanding of relationships between the physical and optical properties of the ice to be able to predict how these properties change and evolve under different climatic conditions. Prediction of apparent optical properties like albedo and transmissivity is complicated by multiple scattering and requires use of a radiative transfer model. Numerous radiative transfer models of varying sophistication and accuracy have been developed for sea ice. These models range in complexity from a simple exponential decay model [*Maykut and Untersteiner*, 1971] to multistream and multilayer treatments [*Grenfell and Maykut*, 1977; *Grenfell*, 1983, 1991; *Perovich*, 1990]. The most comprehensive model is the multistream treatment of radiative transfer in an ocean-ice-atmosphere column [*Jin et al.*, 1994]. While these models require information about the spectral and angular distribution of the incident radiation and about other boundary conditions, the principal uncertainties are related to the inherent optical properties (IOPs) which describe absorption and scattering in the ice. The magnitudes and vertical variation of these IOPs are determined by the ice microstructure which is composed of numerous inclusions of brine, gas, precipitated salt crystals and other impurities embedded in a matrix of pure ice. This structure is complex and the effects of different inclusions on the optical properties of the ice are difficult to determine. The objective of this study is to develop a more quantitative understanding of how the type and distribution of these inclusions affect inherent and apparent optical properties of the ice. Investigation of these relationships is made possible through the development and validation of a specialized "structural-optical" model for sea ice.

2. Background

[5] The visual appearance of sea ice, from bright white to milky or translucent gray, is indicative of significant multiple scattering. Direct measurements of inherent optical properties, including the scattering coefficient (σ), scattering phase function (characterized by the asymmetry parameter, g), and absorption coefficient (κ), are difficult to make within multiply scattering media. One approach for obtaining these IOPs is to calculate them directly from information on the microstructure of the ice. The IOPs can then be incorporated into radiative transfer models and tested using measurements of apparent optical properties (AOPs).

[6] A theoretical framework relating the physical properties of sea ice to the IOPs was laid out by *Grenfell* [1983]. In this formulation, sea ice was modeled as a three-phase system consisting of pure ice, precipitated salt crystals, liquid brine inclusions, and gas bubbles. Absorption in sea ice was attributed to the pure ice matrix, the bulk brine volume fraction, and any particulate or biological inclusions present; scattering was assumed to be caused primarily by inclusions of brine, gas, and precipitated salts found within the ice [*Grenfell*, 1983, 1991]. It was assumed that the individual inclusions scatter independently so that κ, σ, and g could be determined for each type of scatterer and combined incoherently.

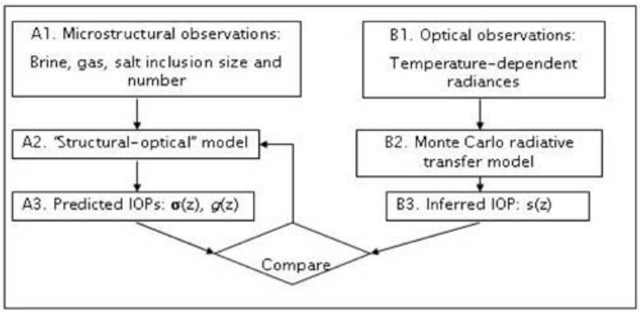

Figure 1. Schematic of experimental approach.

[7] Inclusions in sea ice occur over a wide range of scales. The largest brine inclusions may be centimeters long, whereas precipitated salt crystals can have edge lengths on the order of microns [*Light*, 1995]. The size, refractive index contrast, and shape of an inclusion dictate how it scatterers light. While these properties vary with inclusion type, they can also depend strongly on ice temperature. Changes in temperature produce changes in the size and salinity of brine inclusions as they adjust to a new freezing equilibrium. The refractive index of brine depends on its concentration [*Maykut and Light*, 1995], as does the precipitation or dissolution of a variety of solid salt crystals [*Nelson and Thompson*, 1954; *Richardson*, 1976].

[8] Because natural sea ice typically exhibits large vertical and horizontal variations in structure, apparent optical properties measured in the field are usually not representative of ice with uniform IOPs, making it difficult to validate structural-optical models using field data. In an effort to address this problem, *Erickson* [2002] collected optical data from samples of laboratory grown sea ice in a temperature-controlled freezer laboratory. Samples were assumed to be isothermal and to have fairly uniform structure. Changes in AOPs were monitored as the sample temperature was first decreased from −15 to −35°C, then increased to −1°C. Large increases in scattering were observed at temperatures below −23°C, presumably because of the precipitation of hydrohalite crystals. Increases in scattering were also observed at very high temperatures. These data provided a unique look at the temperature-dependent changes in the optical properties of sea ice but were not accompanied by detailed structural observations. In this paper we present results from studies where the microstructure and the optical properties of natural sea ice samples were monitored simultaneously, the ultimate goal being the development of a physically-based, structural-optical model.

3. Approach

[9] To lay the groundwork for this model, we designed laboratory experiments to quantify relationships between the structural and optical properties in natural sea ice (see Figure 1). Structural and optical data were collected concurrently in a temperature-controlled freezer laboratory using two isothermal samples of interior, first-year ice taken

from adjacent locations in the same ice core. Varying the temperature of these samples produced large structural changes, allowing us to document the optical response of the ice under a wide range of conditions. Optical samples 5 cm in length were taken from the middle of the core where visual inspection indicated that the ice was relatively homogeneous. Observations of the microstructure (Figure 1, A1) were made on vertical and horizontal thin sections using a high-resolution zoom lens and a black and white digital video camera. Numerous images were recorded, detailing the size and number density of brine tubes, brine pockets, gas bubbles, and to a limited extent, precipitated salt crystals. The various inclusions were counted and their size distributions parameterized. An equivalent spheres treatment [*Grenfell and Warren*, 1999] was applied and a temperature-dependent effective cross-sectional area $\psi(T)$ estimated for each type of inclusion. Details of the observations and results are described in *Light et al.* [2003a].

[10] Concurrent AOP observations (B1) were made on cylindrical core sections 10 cm in diameter and 5 cm thick. Transmitted, backscattered, and side scattered spectral radiances were recorded at temperatures between −1 and −35°C. Temperature was normally varied in 2–5°C increments, and the ice allowed to equilibrate for at least 24 hours before new measurements were made.

[11] Optical measurements were interpreted using a two-dimensional Monte Carlo model (B2) developed specifically to treat radiative transfer in multiply scattering, cylindrical domains [*Light et al.*, 2003b]. Observed radiances were interpreted using a similarity principle developed by *van de Hulst* [1980] who defined a dimensionless similarity parameter, S, as

$$S = [1 + (\sigma/\kappa)(1 - g)]^{-1/2}.$$

He showed that the apparent optical properties for highly scattering, optically thick media are nearly the same for a wide range of IOP values, as long as they combine to give the same value of S. We will refer to this as the "similarity principle". For similarity comparisons where κ does not change, it is convenient to introduce a reduced similarity parameter s, where

$$s = \sigma(1 - g).$$

Since κ for pure ice is known to a high degree of accuracy, and does not vary over the temperatures considered in these experiments, we will normally use s in the work described below. Note that s has the same dimensions as σ, m^{-1}. For a particular absorption coefficient, two domains with the same s, but different σ and g, have nearly identical AOPs. Because s represents the effects of both σ and g, s can be thought of as a scattering invariant, such that relative levels of scattered radiation can be compared. By exploiting similarity, radiance observations can be compared directly with model simulations without specifying unique values of σ and g.

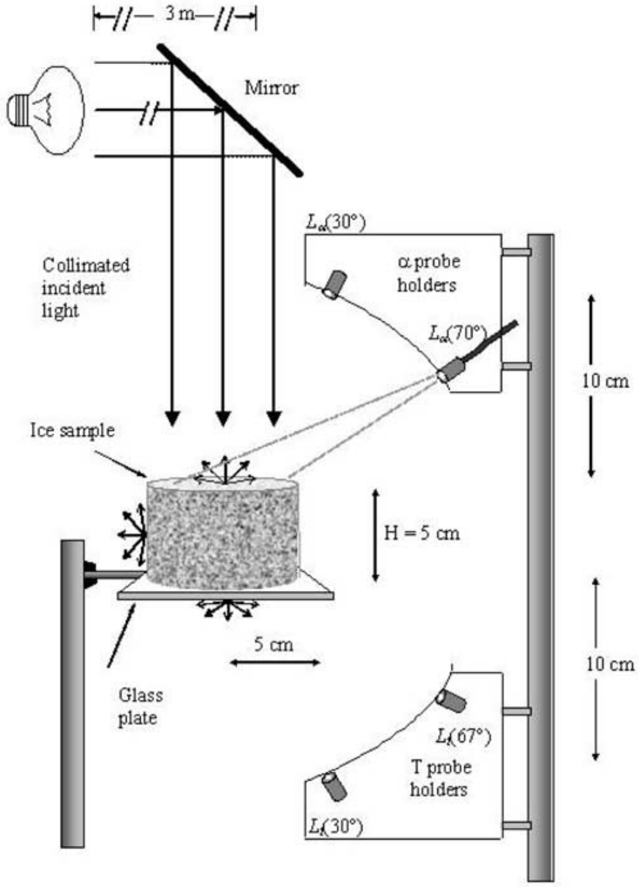

Figure 2. Schematic showing the configuration of incident light, sample, and detector used to collect the optical data.

[12] The structural-optical model (A2) developed here is based on the theoretical framework of *Grenfell* [1983]. The model uses direct observations of inclusion number densities and size distributions obtained from microstructural imagery to predict $\kappa(T, \lambda)$, $\sigma(T)$, and $g(T)$ for brine inclusions, gas bubbles, and precipitated salt crystals. For sea ice without significant quantities of impurities, such as was used in this study, $\kappa(T, \lambda)$ is taken to be independent of temperature, and to be equal to $\kappa(\lambda)$ for pure ice. Ultimately, changes in gas and brine volume affect the bulk value of $\kappa(T, \lambda)$, but those small changes are assumed to be negligible here. Fundamental physical relationships between the ice structure and its optical properties are deduced by iteratively comparing values of s derived from AOP data (B3) with values of s predicted with the structural-optical model (A3). These comparisons will allow the model to be refined and improved.

4. Optical Measurements

[13] Samples for the optical observations were prepared at −15°C. Cylinders 5 cm in height (H) and 10 cm in diameter were cut from depths of 70–90 cm within first-year ice cores extracted from the Beaufort Sea near Pt. Barrow, AK. The top and bottom faces of the cylinder were initially cut with a band saw and then microtomed. The sidewalls of the core were hand polished to remove any frost accumulation. Apparent optical property measurements were made by illuminating the top surface of the cylindrical sample with normally-incident, approximately collimated white light (Figure 2). A 500 watt incandescent bulb was mounted in a parabolic reflector with a glass faceplate, ~3 meters

horizontally from the sample. By placing the light source as far from the sample as possible within the laboratory, the sample surface presented a small solid angle to the incident light, causing light incident on the sample to be approximately collimated. A mirror set at a 45° angle reflected the light vertically downward onto the top surface of the sample. The sample rested on a 3 mm thick transparent glass plate. Black baffling was used to reduce stray light reaching the sample surfaces.

[14] Measurements of diffuse light backscattered and transmitted by the sample were made using a single fiber optic probe that could be positioned to monitor 5 different radiances: backscattered at 30° ($L_{\alpha 30}$) and 70° ($L_{\alpha 70}$) from zenith, transmitted at 30° (L_{t30}) and 67° (L_{t67}) from nadir, and sidescattered radiance (L_s) normal to the side surface at H/2. Transmission measurements were made at 67° instead of 70° to avoid interference from the instrument housing. These particular zenith and nadir angles were selected because they are the ordinate angles for a 4-point Gaussian quadrature (see equation (1)).

[15] All measurements were made with the same probe to avoid intercalibration problems. The probe was coupled to a Spectron Engineering spectrophotometer (Model SE 590) which recorded light at wavelengths between 400 and 1000 nm with a spectral resolution of ~3 nm. A personal computer was used to run the instrument and record spectrophotometer output. The optical probe was designed to have a narrow field of view so that it could be used to monitor radiance. The radiance probe was fitted with a collimating lens so that the footprint did not extend beyond the boundaries of the sample.

[16] Since the objective of the AOP measurements was comparison with the radiative transfer model, absolute radiometric measurements were not necessary, and the probe assembly was calibrated so that relative radiance measurements could be made. A target made of Spectralon®, a material with precisely known spectral albedo (α_{cal} = 0.99 at visible wavelengths) was used to both calibrate the probe and monitor the incident irradiance. The albedo of the target is given by

$$\alpha_{\mathrm{target}} = 0.99 = \frac{\int_{2\pi} \tilde{L}(\theta)\cos(\theta)d\Omega}{\int_{2\pi} L_{inc}(\theta)\cos(\theta)d\Omega},$$

where $\tilde{L}(\theta)$ is the axially-symmetric radiance field backscattered from the target and dΩ is the solid angle element over which the radiance field is integrated. Total backscattered irradiance from the target can be estimated from radiance measurements $\tilde{L}'_i$ made at specified angles θ_i using a Gaussian quadrature:

$$\int_{2\pi} \tilde{L}(\theta)\cos(\theta)d\Omega \approx 2\pi\sum_i a_i\mu_i x\tilde{L}'_i, \qquad (1)$$

where $\mu_i = \cos\theta_i$, a_i are known quadrature weighting factors [*Abramowitz and Stegun*, 1965], and x represents the unknown probe throughput which accounts for differences between measured and actual radiances resulting from probe optical characteristics and experiment geometry, i.e., $\tilde{L} = x\tilde{L}'$. Measured radiances L'_i emanating from the surface of the ice at the quadrature angles can likewise be used to estimate the backscattered irradiance from the ice sample:

$$\int_{2\pi} L(\theta)\cos(\theta)d\Omega \approx 2\pi\sum_i a_i\mu_i xL'_i$$

The following expression shows how the relative (normalized by the incident irradiance) radiance $\hat{L}_i$ can be calculated from the measured radiance L'_i, the value of α_{target}, and measurements of backscattered radiance from the target:

$$\hat{L}_i = \frac{xL'_i}{\int_{2\pi} L_{inc}\cos(\theta)d\Omega} = L'_i\frac{\alpha_{target}}{2\pi\sum_i a_i\mu_i\tilde{L}'_i}.$$

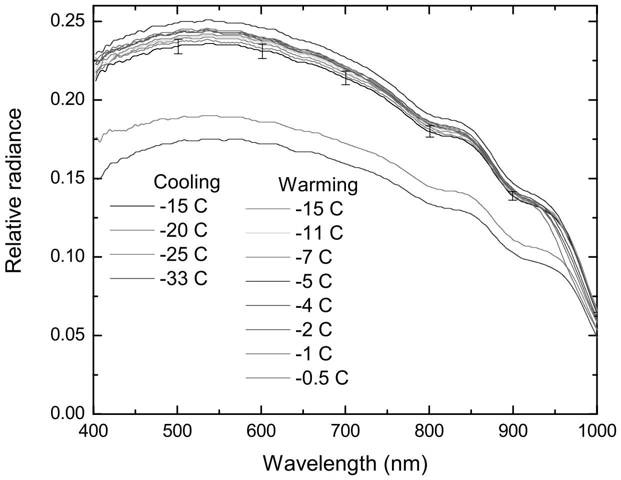

Figure 3. Temperature-dependent changes in spectral radiance transmitted at 30° from nadir. Radiances were measured through the glass plate used to support the sample, then normalized by the incident irradiance. See color version of this figure at back of this issue.

[17] Each time optical measurements were made, the calibration target was initially positioned over the sample and $\tilde{L}'_{\alpha 30}$ and $\tilde{L}'_{\alpha 70}$ recorded. The target was then removed to allow measurement of $L'_{\alpha 30}$, $L'_{\alpha 70}$, L'_{t30}, L'_{t67}, and L'_s. Finally, the target was replaced and a second calibration carried out to verify the stability of the source during the measurement sequence. An empirical correction of 4% was made to account for the difference in distance between the probe and the surfaces of the calibration target and ice sample.

[18] Data on spectral radiances were recorded for the optical sample as it was progressively cooled from −15 to −20, −25, and −33°C, then warmed to −15, −11, −7, −5, −4, −2, and −1°C. Typical results are illustrated by the transmission spectra $L_{t30}(\lambda, T)$ shown in Figure 3. Error bars shown on the T = −15°C curve indicate uncertainties of ±2%, estimated from the standard deviation of a series of repeated radiance measurements. This variability resulted primarily from random errors associated with the position of the probe within the probe holders. Normalized $L_{t30}(\lambda, T)$ radiance maxima generally occurred at 530–545 nm and

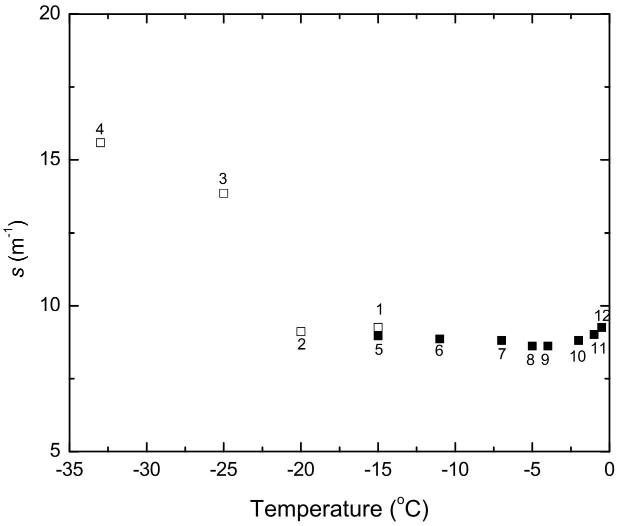

Figure 4. Derived values of the similarity parameter *s* as a function of temperature. Values were derived from observed radiances by comparison with Monte Carlo model calculations.

peak values ranged from 0.175 at −33°C to 0.251 at −5°C. Radiances recorded at lower temperatures showed large variability; those recorded at high temperature tended to be more tightly clustered. All transmitted radiances were measured through the glass plate used to support the sample.

[19] After optical measurements were completed, bulk physical properties were determined for the sample. The salinity and density of the optical sample were measured to be 4.7 ppt and 0.915 ± 0.020 Mg m^{-3}, respectively. These values, used in conjunction with the equations of freezing equilibrium [*Cox and Weeks*, 1983], gave a brine volume (V_b) of 1.9% and a gas volume (V_g) 0.95% at −15°C.

[20] The 2-D Monte Carlo radiative transfer model (MCM) was the primary tool used to derive IOPs from the optical measurements. The ice sample was modeled as a refractive cylinder with spatially uniform σ, κ_λ, and g, while the supporting glass plate was modeled as a non-scattering second layer with a refractive index of 1.50 and a spectral absorption coefficient that was estimated with a simple transmittance measurement in the laboratory. It was initially assumed that scattering in the ice could be described by a *Henyey and Greenstein* [1941] phase function with $g = 0.95$. The MCM was used to calculate $L_{\alpha 30}$, $L_{\alpha 70}$, L_{t30}, L_{t67}, and L_s for a wide range of s values. Observed radiances were then compared with the predicted radiances, and the value of s that best explained all five observed spectra was selected at each temperature. Details of the selection criteria are given by *Light et al.* [2003b]. Derived values for $s(T)$ are shown in Figure 4. The cooling sequence is indicated by open symbols and the warming sequence by solid symbols. Both sequences were initiated at −15°C. Symbol numbers indicate the order in which measurements were made. The overall range of s varied from 8.6 m^{-1} at −5°C to 15.6 m^{-1} at −33°C. This is almost a two-fold change in scattering attenuation. Uncertainties are estimated to be approximately the symbol size.

[21] Three distinct temperature regimes can be identified in Figure 4. (1) $T < -23°C$: Values of s increased by nearly 70% as the sample was cooled between −20 and −33°C. Such strong increases in attenuation by scattering were almost certainly the direct result of the precipitation of hydrohalite crystals which should begin to occur at −22.9°C. (2) $-23°C < T < -8°C$: Attenuation due to scattering at intermediate temperatures appeared to be almost constant. Between −15 (point 5) and −5°C (point 8), for example, s changed by less than 5%. Two competing factors appear to contribute to this behavior. As sea ice warms across this temperature regime, there are moderate increases in scattering due to increased brine and gas volume. At the same time, there are decreases in scattering due to the decreasing mass of precipitated mirabilite crystals. To a large extent, these effects appear to counteract one another. Scattering by mirabilite crystals eventually ceases above −8.2°C, where all mirabilite crystals should completely dissolve. (3) $T > -8°C$: At temperatures above the mirabilite precipitation (points 7–12), attenuation due to scattering decreased slightly as the sample was warmed to −4°C (point 9), then increased monotonically as the temperature approached −1°C (point 12). The total increase in s was less than 10% between −8°C and −1°C, although the ice experienced an eight-fold increase in brine volume and an almost two-fold increase in gas volume. Such large increases in brine and gas volume were expected to produce correspondingly large increases in scattering, but the observed optical changes were surprisingly small.

5. Structural-Optical Relationships

[22] In this section we develop explicit relationships between the microstructure of the ice and the inherent optical properties of each type of included scatterer. We also describe how these relationships are used to predict values of κ, σ, and g for the entire sample. These relationships constitute the structural-optical model.

5.1. Absorption Coefficient, κ

[23] The total absorption coefficient at any wavelength, $\kappa_{\mathrm{total}}(\lambda)$, can be written as the volume-weighted sum of the individual absorption coefficients ($\kappa_j[\lambda]$) of pure ice, included brine, precipitated salts, and included particulates [*Grenfell*, 1991]:

$$\kappa_{\mathrm{total}}(\lambda) = \kappa_{\mathrm{ice}}(\lambda)V_{\mathrm{ice}} + \kappa_{\mathrm{brine}}(\lambda)V_{\mathrm{brine}} + \kappa_{\mathrm{ps}}(\lambda)V_{\mathrm{ps}} + \kappa_{\mathrm{particulates}}(\lambda)V_{\mathrm{particulates}}. \tag{2}$$

where V_j is fractional volume. Because the samples used in this study did not generally contain absorbing particulates, $V_{\mathrm{particulates}}$ was assumed to be zero. Since information on absorption by the precipitated salts was not available and since V_{ps} is very small relative to V_{ice} and V_{brine}, effects of κ_{ps} on total absorption were also assumed to be negligible, hence

$$\kappa_{\mathrm{total}}(\lambda) \approx \kappa_{\mathrm{ice}}(\lambda)V_{\mathrm{ice}} + \kappa_{\mathrm{brine}}(\lambda)V_{\mathrm{brine}}.$$

Because V_{ice} is usually much larger than V_{brine} and because $\kappa_{\mathrm{ice}}(\lambda)$ is close to $\kappa_{\mathrm{brine}}(\lambda)$, $\kappa_{\mathrm{total}}(\lambda)$ is approximately equal to $\kappa_{\mathrm{ice}}(\lambda)$. $\kappa_{\mathrm{ice}}(\lambda)$ is strongly wavelength-dependent, with values of less than 0.05 m^{-1} at blue wavelengths, increasing to more than 10 m^{-1} in the near infrared.

5.2. Scattering Coefficient, σ

[24] Scattering for the observed distributions of brine tubes, brine pockets, gas bubbles, and precipitated salt crystals in the microstructure imagery was characterized by computing the temperature-dependent equivalent cross-sectional area for each type of inclusion,

$$\psi(T) = \pi \int_{r_{\min}}^{r_{\max}} r_{eq}^{2}(T) N\left(r_{eq}, T\right) dr_{eq}$$

where r_{eq}(T) is the temperature-dependent equivalent spherical radius and $N(r_{eq}, T)$ is the number density of the corresponding equivalent spheres [*Light et al.*, 2003a]. Note that the units of this number-density weighted area are inverse length. The formulation is based on the theory of equivalent spheres [*Grenfell and Warren*, 1999] where a scatterer is represented by a collection of spheres such that both the total volume and total surface area of the original inclusion are conserved. Scattering inclusions in sea ice can be roughly classified as spherical, prolate ellipsoidal, tubular or as individual geometric crystal shapes. For inclusions that are approximately spherical (e.g., most gas bubbles), r_{eq} and $N(r_{eq})$ are equal to the observed radius and number density. For ellipsoidal and cylindrical inclusions where the length-to-diameter aspect ratio γ is less than 6, $N(r_{eq})$ can be up to three times larger than the observed number density; for cylindrical inclusions where γ = 60, $N(r_{eq})$ can be more than 25 times the actual number density.

[25] The temperature-dependent scattering coefficient for each type of inclusion is given by:

$$\sigma(T) = \int_{r_{\min}}^{r_{\max}} Q_{sca}\left(r_{eq}\right) \pi r_{eq}^{2}(T) N\left(r_{eq}, T\right) dr_{eq} \qquad (3)$$

where $Q_{sca}(r_{eq})$ is the scattering efficiency. All the inclusions considered here (i.e., brine, gas and salt crystals) have sizes much larger than the wavelength, so that Q_{sca} is approximately equal to 2, and $\sigma(T) \approx 2 \cdot \psi(T)$. The calculation of σ(T) for each type of inclusion is described below.

5.2.1. Brine Inclusions

[26] Both the number density (N_{brine}) and the aspect ratio γ of brine inclusions were observed to depend on the vertical extent (l) of the inclusions and to be well represented by power laws [*Light et al.*, 2003a]:

$$N_{brine}(l) = 0.28\ l^{-1.96}, \quad 0.01 \text{ mm} < l < 8 \text{ mm} \qquad (4)$$

and

$$\gamma(l) = 10.3\ l^{0.67}, \qquad 1 \leq \gamma \leq 70 \text{ and } l > 0.03 \text{ mm}$$

$$\gamma(l) = 1 \qquad l \leq 0.03 \text{ mm}$$

where l is given in mm and N_{brine} in mm^{-3}. Brine inclusions were arbitrarily divided into "pockets" and "tubes". Pockets were assumed to have l < 0.5 mm and were represented as prolate ellipsoids, while tubes ($l \geq 0.5$ mm) were represented as right circular cylinders.

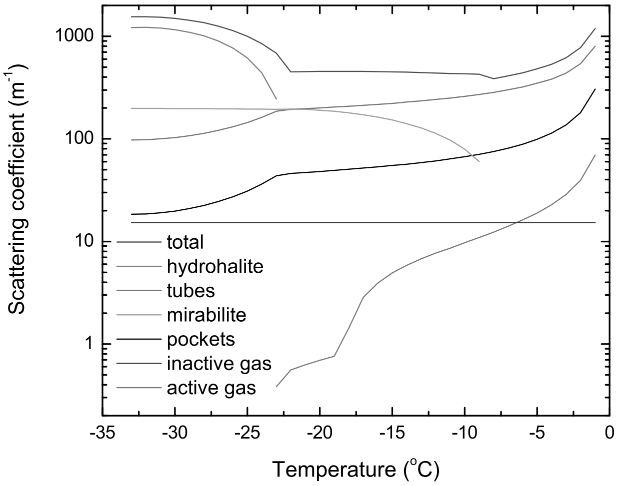

Figure 5. Temperature-dependent scattering coefficients for various types of scatterers in sea ice as predicted by the structural-optical model. See color version of this figure at back of this issue.

[27] The total value of ψ_{brine} for all brine inclusions observed in the thin section imagery at −15°C was estimated to be 110 m^{-1}, with 30 m^{-1} being contributed by the pockets (ψ_{bp}) and 80 m^{-1} by the tubes (ψ_{bt}) [*Light et al.*, 2003a]. However, the brine volume observed in the microstructure sample (V_{brine} = 1.2%) was only 60% of that calculated for the optical sample at −15°C. The most likely explanation is that the thin section did not contain many of the larger and more widely dispersed brine tubes present in the core. Such features would, of course, lead to greater scattering in the optical sample. To estimate the effect on ψ_{bt}, we assumed that these larger tubes followed the same size distribution given by equation (4). We found that extending $N_{\text{brine}}(l)$ from l = 8 mm to include tubes up to 14.6 mm in length produced a brine volume of 1.9%, in agreement with the optical sample. This increased $\psi_{\text{bt}}(-15°\text{C})$ from 80 to 110 m^{-1}, and yielded estimates for $\sigma_{\text{bp}}(-15°\text{C})$ of 60 m^{-1} and $\sigma_{\text{bt}}(-15°\text{C})$ of 220 m^{-1}.

[28] Temperature-dependent volume changes for each brine inclusion were predicted from the equations of freezing equilibrium [*Cox and Weeks*, 1983]. Volume increases were assumed to be proportional to the initial size of the inclusion. Pockets were assumed to grow and shrink in length and diameter, retaining constant aspect ratio; tubes were assumed to grow and shrink in diameter and aspect ratio, retaining constant length. These rules constitute our structural model for brine inclusions. Application of this model to the scattering coefficients obtained at −15°C allow calculation of $\sigma_{\text{bp}}(T)$ and $\sigma_{\text{bt}}(T)$. The results (Figure 5) indicate that scattering by brine tubes in interior, first-year ice is roughly 4–5 times that of brine pockets at all temperatures. As temperature increases, so does the contribution of brine inclusions to the total scattering coefficient.

5.2.2. Gas Bubbles

[29] There are two types of gas bubbles in sea ice: (1) active bubbles contained in brine inclusions whose size

varies with changes in the size of the brine inclusion, and (2) inactive bubbles trapped in the ice lattice whose size remains constant with temperature. As before, scattering by gas bubbles in brine inclusions was first computed directly from observed size and number distributions at −15°C. Somewhat unexpectedly, only a fraction of the brine inclusions were found to contain bubbles at this temperature. Estimates of the total number density of active bubbles N_{bubble} were based on the percentage of brine inclusions containing bubbles and on the gas volume fraction of these inclusions. The fraction of brine pockets (f_{bp}) and tubes (f_{bt}) containing bubbles was observed to be 10% and 40%, respectively. Typical fractional gas volumes for these brine inclusions were estimated to be 10% for pockets ($v_{\mathrm{bub\text{-}bp}}$) and 3% for tubes ($v_{\mathrm{bub\text{-}bt}}$) at −15°C. As the temperature of the sample increases, some of the pure ice (density ≈ 0.917 Mg m^{-3}) around each brine inclusion melts to become brine with density greater than 1.0 Mg m^{-3}. It was assumed that any existing gas bubble would expand to fill the difference in volume. Changes in gas bubble size with temperature thus depend on changes in the volume of the associated brine inclusion, information which can be obtained from the freezing-equilibrium relations [*Cox and Weeks*, 1983].

[30] It should be noted, however, that temperature-dependent changes in the size of active bubbles also depend on the actual volume of the host brine inclusion. This is simply illustrated by considering two identical gas bubbles, one in a large brine inclusion and the other in a small brine inclusion. Upon warming, both brine inclusions increase their volume by the same percentage, meaning that a larger volume of ice would melt around the large brine inclusion than the small one. Hence, the size of the bubble in the larger inclusion would increase more than the one in the smaller inclusion, making the temperature-dependent behavior of the bubble size distribution dependent on the brine inclusion size distribution. This effect is taken into account in this model. By specifying f_{bp}, f_{bt}, $v_{\mathrm{bub\text{-}bp}}$, and $v_{\mathrm{bub\text{-}bt}}$ at −15°C, the active bubble distribution can be manipulated to simulate enlarging and shrinking as the ice is warmed and cooled. Changes in the volume of an individual active bubble are

$$V_{\mathrm{bubble\text{-}a}}(T) = V_{\mathrm{bubble\text{-}a}}(-15^{\circ}\mathrm{C}) + \Delta V_{\mathrm{brine}}\left(\frac{\rho_{\mathrm{brine}}(T)}{\rho_{\mathrm{ice}}} - 1\right),$$

where $\mathrm{V}_{\mathrm{bubble\text{-}a}}$ is the volume of the active bubble, $\Delta V_{\mathrm{brine}}$ is the fractional change in volume of the host brine inclusion between −15°C and T, as specified by freezing equilibrium; $\rho_{\mathrm{brine}}(T)$ varies between 1.03 Mg m^{-3} at −2°C and 1.23 Mg m^{-3} at −34°C, as given by *Maykut and Light* [1995]; and the density of pure ice ρ_{ice} (Mg m^{-3}) = 0.917 − 1.403 × $10^{-4}T$ (°C) [*Pounder*, 1965]. In this treatment, the number density of active bubbles is assumed to remain constant with temperature.

[31] For the purpose of calculating ψ and σ, bubbles are assumed to be spherical at −15°C. At higher temperatures, however, bubbles in tubes frequently become large enough that their spherical dimensions exceed the tube diameter. When the bubble diameter grows larger than the tube diameter, the diameter of the bubble becomes fixed at the tube diameter, the shape of the bubble is assumed to be cylindrical, and the bubble is permitted to grow in length only. For such tubular bubbles, $\psi_{\mathrm{bubble\text{-}a}}$ and $\sigma_{\mathrm{bubble\text{-}a}}$ are calculated using the equivalent spheres treatment, in the same manner as brine inclusions. The predicted $\sigma_{\mathrm{bubble\text{-}a}}(\mathrm{T})$ for all active gas bubbles is shown in Figure 5. Although much smaller in magnitude, it is more sensitive to temperature than either tubes or pockets, showing large increases in scattering as the temperature increases above −10°C.

[32] With $f_{\mathrm{bp}} = 0.1$, $f_{\mathrm{bt}} = 0.4$, $v_{\mathrm{bub\text{-}bp}} = 0.1$, and $v_{\mathrm{bub\text{-}bt}} = 0.03$, the fractional volume of active gas in the optical sample is computed to be 0.00024 at −15°C, ~2% of the total gas volume indicated by the density and salinity measurements. It appears that there must have been additional gas or void space in the optical sample that was not recorded in the structural observations reported by *Light et al.* [2003a]. These inclusions are important because of their large refractive index contrast with the surrounding ice. Reexamination of the imagery used to characterize the microstructure revealed previously unidentified features that are probably inactive gas bubbles embedded in the ice, e.g., see features highlighted in the lower right hand corner of Figure 6. The effective diameters of these bubbles range from 0.09 to 0.21 mm with a number density of ~0.24 mm^{-3}, indicating that the value of ψ for inactive gas ($\psi_{\mathrm{bubble\text{-}i}}$) at −15°C is 7.6 m^{-1} and σ for inactive gas ($\sigma_{\mathrm{bubble\text{-}i}}$) at −15°C is 15.2 m^{-1} in this thin section. These values should remain constant with temperature, as assumed in Figure 5.

[33] The fractional gas volume from the inactive bubbles observed in this image was estimated to be 0.00215. This, combined with the volume of active gas, still only accounts for 25% of the total predicted gas volume. We will attempt to quantify the gas content of the optical sample more precisely when we present the comparison of optical and structural data in Section 6.4.1.

5.2.3. Precipitated Salt Crystals

[34] There are two types of precipitated salts that significantly affect radiative transfer in sea ice: (1) mirabilite crystals that form below −8.2°C and (2) hydrohalite crystals that form below −22.9°C. Numerous examples of mirabilite crystals were observed in brine tubes and larger pockets. Crystals in smaller pockets were not readily apparent, probably because they were very small (<10 μm) and could not be resolved by our imaging system. Observed crystal sizes in the larger inclusions ranged from 15 μm to 140 μm diameter. *Light et al.* [2003a] estimated that $\psi_{\mathrm{mirabilite}}(-15^{\circ}\mathrm{C}) = 48.7\ \mathrm{m}^{-1}$ in the 3 ppt thin section sample. This estimate was based on the simple assumption of an effective crystal edge length of 10 μm since direct measurement of the size distribution was not feasible.

[35] With a salinity of 4.7 ppt, the optical sample should contain $9 \cdot 10^{-4}$ kg of mirabilite per kg of sea ice at −15°C [*Richardson*, 1976]. Assuming a crystal edge length of 10 μm, $\psi_{\mathrm{mirabilite}}(-15^{\circ}\mathrm{C}) = 76.3\ \mathrm{m}^{-1}$ and $\sigma_{\mathrm{mirabilite}}(-15^{\circ}\mathrm{C}) = 152.6\ \mathrm{m}^{-1}$. The value of $\sigma_{\mathrm{mirabilite}}(\mathrm{T})$ is shown in Figure 5, where the temperature dependent total mass was based strictly on freezing equilibrium, and the crystal edge length was held constant at 10 μm. The assumption of constant crystal size was made despite the observation that existing mirabilite crystals grew in size while additional crystals nucleated. This observation, however, does not preclude the possibility of a temperature-independent effective crystal size.

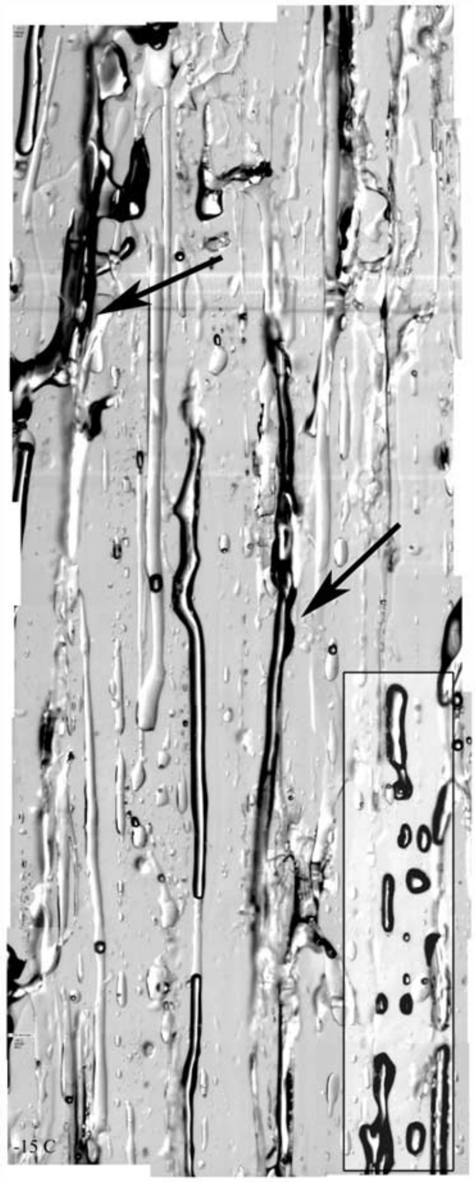

Figure 6. Photomosaic of thin section used for microstructural analysis at T = -15°C. Overall dimensions of the scene are 12.1 mm by 4.7 mm. The highlighted area includes 13 inactive gas bubbles. Arrows point to drained brine tubes. Figure from *Light et al.* [2003a].

[36] Figure 5 suggests that changes in scattering due to mirabilite are roughly balanced by opposite changes related to brine inclusions and active gas bubbles. As the ice warms, mirabilite crystals dissolve and their scattering diminishes, while brine inclusions and active gas bubbles enlarge and their scattering is enhanced. Our experimental results suggest that this balance may be independent of ice type and details of the microstructure. If ice salinity is increased, for example, σ for all the inclusions present will increase due to greater brine volume and mass of precipitates, but relative changes with temperature still act to offset one another.

[37] Although hydrohalite crystals should be present in brine inclusions when T < -22.9°C, they were apparently also too small to be seen in the thin section imagery. However, the increased scattering below -22.9°C (Figure 4) indicates that significant amounts of hydrohalite did precipitate in the optical sample. To calculate $\sigma_{\mathrm{hydrohalite}}(\mathrm{T})$, we again assumed that temperature dependence was based strictly on the freezing equilibrium mass fraction and that crystal size remained constant at 10 μm (Figure 5). Because brine and gas volumes are small at the low temperatures where hydrohalite precipitates, the amount of scattering produced by brine tubes, pockets, and active gas bubbles is small relative to the scattering by hydrohalite crystals.

5.3. Phase Functions

[38] The phase function describes the angular redistribution of light resulting from scattering. For inclusion sizes relevant to this study, g is approximately independent of inclusion size, but depends strongly on the real refractive index (m) of the inclusion relative to its environment (m_{rel}). Relative refractive indices of brine in ice, gas in brine, mirabilite in brine, and hydrohalite in brine are shown in Figure 7a. Because m_{brine} depends strongly on temperature [*Maykut and Light*, 1995], g for an inclusion depends on temperature when brine is either the scatterer (e.g., brine in ice) or the background medium (e.g., gas or salt crystals in brine). The g values vary between -1 (complete backward scattering) and +1 (complete forward scattering). For a particular inclusion size, the value of g is smallest when $|m_{rel} - 1|$ is largest. In this case, backscattering is largest for gas in brine, although gas bubbles in ice scatter almost as effectively. For hydrohalite and mirabilite crystals in brine pockets, $|m_{rel} - 1|$ is largest at their temperatures of initial precipitation since $m_{\mathrm{mirabilite}}$ and $m_{\mathrm{hydrohalite}}$ are assumed to be constant and m_{brine} increases with decreasing temperature. In fact, mirabilite crystals in brine have $|m_{rel} - 1| \approx 0$ at -30°C, so that they become essentially invisible at this temperature. For brine inclusions in ice, $|m_{rel} - 1|$ is largest at low temperatures. As sea ice warms and the brine becomes less concentrated, $|m_{rel} - 1|$ for brine in ice decreases, causing brine inclusions to become increasingly forward scattering.

[39] Mie theory was used to calculate phase functions for brine inclusions in ice, gas inclusions in ice, gas inclusions in brine, and precipitated salt crystals in brine, assuming that all could be represented by equivalent spheres. Representation of the phase function by its asymmetry parameter g (the cosine-weighted angular integral) permitted qualitative comparison of relative amounts of forward and backward scattering between different types of scatterers (Figure 7b) and was used in the model to specify the Henyey-Greenstein scattering phase function. Typical inclusion sizes observed in the thin section were chosen for the calculation, although none of the predicted values were sensitive to size. Scattering by brine and salt inclusions is clearly very forward-peaked (larger g), while gas bubbles produce considerably more backscattering (smaller g). Based on these calculations, desalinated, bubbly ice would be expected to have a bulk g value in the vicinity of 0.86, whereas the first-year interior ice used in this study had a representative g value in the 0.98–0.99 range. Figure 7c shows $(1 - g)$, which is proportional to s. It can be seen that brine inclusions in ice contribute more than 5 times as much to s at -33°C as at -1°C, and that $(1 - g)$ attributable to

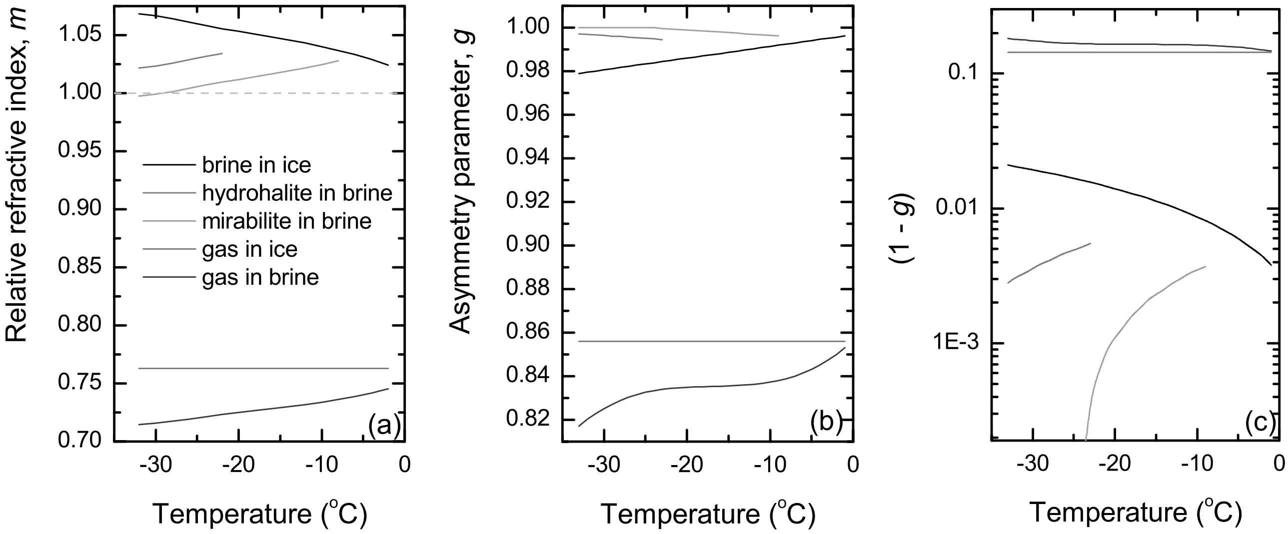

Figure 7. Temperature dependence of (a) relative refractive index, (b) asymmetry parameter, *g*, and (c) [1 − *g*] for inclusions of brine in ice, gas in ice, gas in brine, mirabilite in brine, and hydrohalite in brine. Asymmetry parameters were calculated using equivalent spheres and Mie theory. See color version of this figure at back of this issue.

brine inclusions decreases by a factor of two between −8 and −2°C. Mirabilite in brine shows an order of magnitude decrease in (1 − *g*) between −8 and −23°C, while total changes for hydrohalite and gas in brine are less than a factor of two.

6. Model Development and Testing

[40] The relationships between ice physical properties and IOPs presented above form the basis for the structural-optical model. We will now discuss the formulation of this model, evaluate it for a preliminary set of conditions, and describe how it was tested and refined.

6.1. Preliminary Model

[41] The model is based on equation (2), which describes the spectral absorption within sea ice, and equation (3), which describes the contribution to scattering for each type of inclusion present. The total scattering coefficient is determined by

$$\sigma_{\text{total}} = \Sigma\sigma_{\text{i}} = \sigma_{\text{bp}} + \sigma_{\text{bt}} + \sigma_{\text{bubble-a}} + \sigma_{\text{bubble-i}} + \sigma_{\text{mirabilite}} + \sigma_{\text{hydrohalite}}. \tag{5}$$

Single-term Henyey-Greenstein phase functions were used to represent scattering phase functions for all scatterers in the ice. We are aware that other, possibly more realistic phase functions exist [e.g., *Mobley et al.*, 2002], but chose to restrict the comparisons in this study to the Henyey-Greenstein function. The temperature-dependent ensemble asymmetry parameter can be written

$$g_{total}(T) = \frac{\sum_i \sigma_i(T) g_i(T)}{\sum_i \sigma_i(T)}, \tag{6}$$

where g_{i}(T) are the asymmetry parameters for each type of scatterer as shown in Figure 7b. These two equations, along with equations 2 and 3 constitute the structural-optical model.

6.2. Initial Test

[42] The model was tested by comparing values of *s*(T) predicted by the model with those derived from the optical data (Figure 4). Modeled *s*(T) values were calculated from

$$s(\text{T}) = \sigma_{\text{total}}(\text{T}) \cdot (1 - g_{\text{total}}(\text{T}))$$

using equations (2), (3), (5), and (6).

[43] Figure 8 shows the first attempt to compare predicted values of *s*(*T*) with those derived from the optical observations. Significant discrepancies between the two exist in all three temperature regimes. An initial assessment suggests

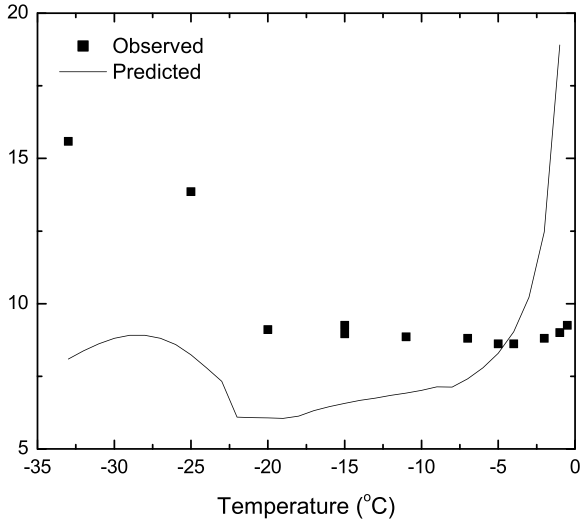

Figure 8. Temperature dependence of observationally-determined similarity parameter compared with values predicted using the preliminary model.

that the discrepancies occur for different reasons in the three regimes. For $T < -22.9°C$, this preliminary treatment significantly underestimates scattering, most likely by hydrohalite crystals. In the intermediate regime where no hydrohalite exists, it appears that improvements in the treatment of scattering by brine inclusions, gas bubbles, and mirabilite crystals are needed. This is not surprising, given that the model accounts for only 25% of the total gas volume in the sample and gas bubbles are highly effective scatterers. It also appears that some important physics may have been omitted when $T > -8°C$ since the model predicts large increases in scattering due to rapid enlargement of brine and gas inclusions while the optical observations show surprisingly little change.

6.3. Model Refinements

[44] This section seeks to improve the preliminary model by addressing problems related to uncertainties in gas volume, scattering by hydrohalite, and inclusion merging.

6.3.1. Gas Volume

[45] The most immediate problem is the estimate of the gas volume of the optical sample, as this potentially impacts the prediction of s at all temperatures. Imagery of the microstructure clearly shows bubbles within brine inclusions and bubbles embedded directly in the ice (Figure 6). The arrows in Figure 6 also point out what appear to be drained brine tubes. At the time of initial analysis, it was assumed that the brine from these tubes had drained during thin section preparation. It is likely, however, that some of these tubes drained when horizontal cuts were made to remove both the thin section and the optical section from the ice core. Drained tubes present in the optical sample should behave as elongated inactive gas bubbles, with negligible temperature-dependent changes in size or scattering. Although these drained tubes might not be normally found in natural ice, they must be taken into account in predicting the optical properties of this sample.

[46] Scattering by drained tubes was modeled by simply adding gas-filled tubes to the ice. The equivalent spheres treatment was applied to the drained tubes in exactly the same way as to the brine-filled tubes (see section 5.2.1). Excellent agreement between the predicted and observed s was obtained at −15°C when the number of drained tubes was set to 3% of the number of brine tubes (Figure 9). This contribution accounted for additional gas volume, bringing the total estimate of gas volume at −15°C to 30% of the volume calculated directly from the density, salinity, and temperature. If the bulk density of the sample were 0.921 Mg m^{-3}, instead of the observed 0.915 ± 0.02 Mg m^{-3}, then the gas bubble parameterization would explain 98% of the predicted gas volume. This density is within the limits of measurement uncertainty.

[47] For comparison, *Mobley et al.* [1998] estimated the amount of scattering within first-year ice sampled in situ off Pt. Barrow, AK at the onset of melt. Their estimates for interior ice between the depths of 0.1 and 1.61 m produced an s value of 4.0 m^{-1}. This value is considerably smaller than our observed values, and the difference may be attributable to the considerable brine drainage that occurred in our laboratory sample. Their measurements were made where the interior ice temperature was −5.7°C, but the ice had salinity of 5.2 ppt and density 0.92 Mg m^{-3}. These physical property measurements are consistent with a general lack of brine drainage.

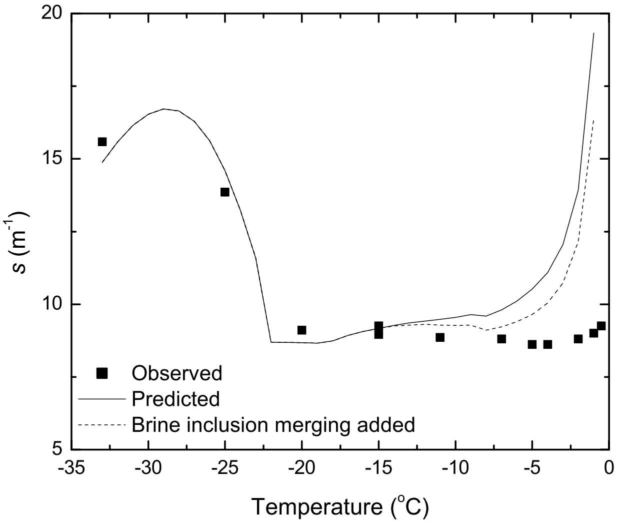

Figure 9. Comparison of observationally determined and predicted values of $s(T)$. A revised model (solid line) includes parameterization of drained tubes and a reduction in the effective size of hydrohalite crystals from 10 to 4.5 μm. The dashed line shows the result of adding the effects of brine inclusion merging to these improvements.

6.3.2. Scattering by Hydrohalite

[48] Even with increased gas volume, the model still fails to produce enough scattering when $T < -23°C$. To match the observations, it is necessary to have increased scattering by the hydrohalite crystals. At this point, details of hydrohalite precipitation patterns have not been investigated. So, as temperature decreases, the model assumes increasing numbers of crystals with a constant effective size of 10 μm. Newly nucleated crystals are presumably very small so it is not unreasonable that the effective size may be considerably less than assumed. By decreasing effective size from 10 μm to 4.5 μm, the associated increase in the surface area of hydrohalite causes $\psi(-33°C)$ to increase from 609 m^{-1} to 1354 m^{-1} and provides a reasonable match to the optical observations (Figure 9). Keeping effective size constant is only one of several possible ways to treat this problem, but more information from higher resolution observations of hydrohalite precipitation in sea ice is needed to develop better treatments.

6.3.3. Brine Inclusion Merging

[49] Even with the improvements described above, there remains a significant discrepancy between predictions and observations at temperatures above −5°C. One likely reason is changes in the distribution of brine and gas inclusions that occurred in the samples as they approached the melting point. Imagery made at high temperatures showed that brine inclusions often merged with neighboring inclusions as they became larger. In some cases, large brine tubes merged with small neighboring inclusions. In other cases, clusters of small pockets merged to form a single inclusion. The net effect of this merging is a reduction in the total surface area of brine-ice interfaces and a corresponding reduction in the ψ functions for brine pockets and tubes.

[50] The effects of merging were included in the model by specifying a reduction in $N_{\mathrm{brine}}(l)$. This was done by (1) calculating the normal increase in the size of each brine inclusion with temperature, (2) reducing the number density for each size to simulate merging, and (3) increasing $l_{\max}$, the upper limit of the size distribution, to conserve total brine volume after merging. Specifically, $N_{\mathrm{brine}}(l)$ at −15°C was first converted to a volume (v) distribution $N_{\mathrm{brine}}(v, -15°\mathrm{C})$ using the assumptions about shape and aspect ratio described in Section 5.2.1. The temperature was then adjusted to T′ and a new volume distribution $N_{\mathrm{brine}}(v, \mathrm{T}')$ calculated using the freezing equilibrium relations of *Cox and Weeks* [1983]. Merging was simulated by

$$\tilde{N}_{\mathrm{brine}}(v, \mathrm{T}') = \eta(v, \mathrm{T}')N_{\mathrm{brine}}(v, \mathrm{T}'),$$

where $\tilde{N}_{\mathrm{brine}}$ is the merged distribution and η is a specified function based on observed merging data. Since merging was never observed below −14°C or in the smallest class of pockets, it was assumed that $\eta(v, \mathrm{T} \leq -14°\mathrm{C}) = \eta(v_{\min}, \mathrm{T}) = 1$, where $v_{\min}$ is the smallest volume in the distribution. The form selected for $\eta(v, \mathrm{T})$ was

$$\log[\eta(v, T)] = \frac{\log(\eta[v_{\max}, T])}{\log(v_{\max}/v_{\min})}\log\left(\frac{v}{v_{\min}}\right), \qquad \text{for } v_{\min} < v < v_{\max}$$

where $v_{\max}$ is the volume of the largest inclusion at temperature T. $\eta(v, \mathrm{T})$ is linear in $\log(v) - \log(N)$ space (see Figure 10), and causes most of the merging to occur in the larger inclusions. $\eta(v_{\max}, \mathrm{T})$, itself, decreases linearly with T, going from 1.0 at −14°C to 0.1 at −1°C, specifically, $\eta(v_{\max}, \mathrm{T}) = 0.0307 - 0.0693\mathrm{T}$, where T is in °C. While this particular parameterization reproduces the general merging behavior observed in the thin section, it is likely that better treatments can be developed when more data become available.

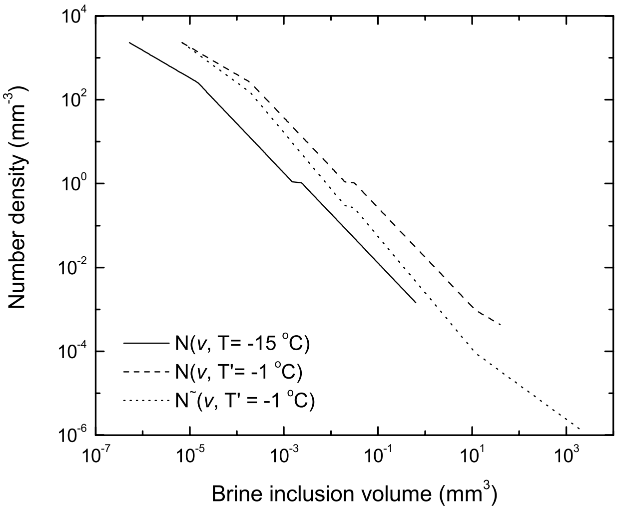

Figure 10. Brine inclusion number distribution as a function of inclusion volume v. $N_{\mathrm{brine}}(v, -15°\mathrm{C})$ was calculated from $N(l)$ (equation (4)) (solid line), while $N_{\mathrm{brine}}(v, -1°\mathrm{C})$ (dashed line) was derived from $N_{brine}(v, -15°\mathrm{C})$ using the freezing equilibrium equations. The merged distribution $\tilde{N}_{\mathrm{brine}}(v, -1°\mathrm{C})$ (dotted line) conserves total brine volume and assumes that $\eta(v_{\max}, -1°\mathrm{C}) = 0.1$. The area under the dashed and dotted curves is identical, as the merging process conserves total brine volume.

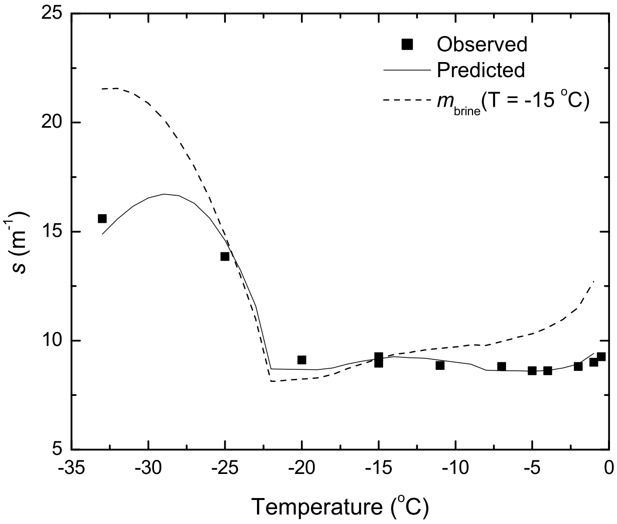

Figure 11. Comparison of observationally determined $s(T)$ values (points) with those predicted by the full model with m_{brine} a function of temperature (solid line) and m_{brine} held fixed at its value at −15°C (dashed line).

[51] To conserve total brine volume in the sample, $\tilde{N}_{brine}(v, \mathrm{T}')$ was extrapolated to larger volumes using the slope of the curve at $v_{\max}$. An example of the effect of merging and volume conservation at T = −1°C is shown in Figure 10. The primary kink in the curves between $v = 10^{-3}$ and 10^{-2} mm^3 marks the transition from pockets to tubes. The predicted effects of merging on $s(T)$ are shown by the dashed line in Figure 9. Clearly, the merging model reduced scattering somewhat at the highest temperatures, but some other mechanism is still needed to explain why scattering does not increase strongly above −5°C.

6.3.4. Gas Bubble Merging and Escape

[52] The rapid increase in brine volume above −5°C is also accompanied by proportional increases in the volume of included vapor bubbles. Unfortunately, observational data are not sufficient to accurately characterize temperature-dependent changes in the distribution of active bubbles. The most probable explanation for the low scattering above −5°C is the upward escape of bubbles as the brine inclusions became larger and increasingly interconnected. Bubbles rising in melt ponds and vapor accumulation beneath the surface of refrozen ponds provide evidence that outgassing is a normal occurrence in warm sea ice, but the extent to which bubble escape from in situ ice is analogous to what happened in the laboratory sample is uncertain. Lacking specific information about the escape process, we simply assumed that all gas bubbles above a certain critical size (r_{c}) were able to escape from the sample. A very good fit to the optical data was obtained with r_{c} = 0.16 mm. Figure 11 shows a comparison between the observed s(T) and values predicted by the full model. Modifications made to the preliminary model produce a full model that closely matches the observed s(T). This full model contains the essential elements of the physical changes observed in the microstructure. These changes include temperature-depen-

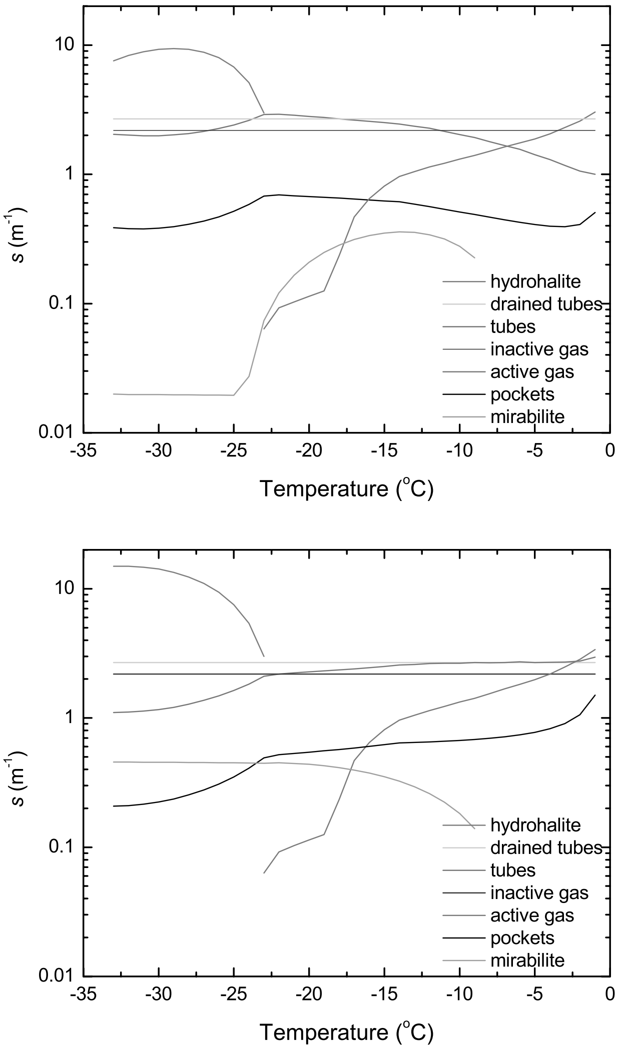

Figure 12. Temperature-dependent partial similarity parameters for each constituent in the full structural-optical model using (a) m_{brine}(T) and (b) m_{brine}(T = −15°C). See color version of this figure at back of this issue.

dent brine inclusion and gas bubble size, brine concentration as prescribed by freezing equilibrium, precipitation of solid salt crystals, brine tube drainage, brine inclusion merging, and escape of active bubbles with radius larger than r_c = 0.16 mm. The relative roles of σ and (1 − g) will be discussed in Section 7, along with sensitivities that affect the model.

7. Discussion

[53] Relationships between the structural and optical properties of sea ice vary with ice temperature and are governed by different constituent scatterers at different temperatures. Figure 12a shows the contributions due to partial s(T) values for each type of scatterer based on the refined model. The values of s(T) in this figure corroborate the optical observations for each temperature regime described in Section 4. Partial s values indicate that scattering at T < −22.9°C is dominated by hydrohalite crystals (magenta curve). In contrast, moderate temperatures are characterized by scattering produced by brine (red and black curves), gas (green curve), and mirabilite crystals (cyan curve). No one constituent dominates changes in scattering at these temperatures. Increases in the size of brine inclusions and active gas bubbles cause scattering coefficients to increase as the ice warms. Dissolution of mirabilite crystals upon warming causes the scattering coefficient for the crystals to decrease. Scattering in this regime remains nearly independent of temperature, the result of an approximate balance between enlarging brine and gas inclusions and dissolving mirabilite crystals. For T > −8.2°C, s for active gas bubbles increases rapidly, and this is manifested in slightly increased scattering in the observed optical properties.

[54] Partial s values for each constituent depend on both the ice microstructure (σ) and its dielectric properties (1 − g). Both the microstructure and the dielectric properties are inextricably tied to the chemistry of freezing equilibrium in seawater. Since freezing equilibrium only dictates the bulk amounts of ice, brine, gas, and precipitated salt that exist at each temperature in the seawater system, it does not dictate a specific distribution of inclusions. A model that depends strictly on the chemistry of freezing equilibrium could be the most widely applicable type of structural-optical model. If such a model were appropriate, the optical properties of the ice could be determined without explicit knowledge of ice type, age, condition, or specific microstructure. To assess the applicability of the structural-optical model developed in this study, we consider the effect of processes governed strictly by freezing equilibrium relative to processes influenced by the ice type or its history.

[55] We begin by assessing the impact of m_{brine}(T) on the full model. We then consider effects of variable ice salinity, and finally the role of specific microstructural configuration.

7.1. Role of m_{brine}(T)

[56] Changes in s that result from variations of m_{brine} with temperature occur regardless of ice type or the exact distribution of inclusions. To illustrate the impact of the temperature-dependent dielectric properties of brine on the optical properties of sea ice, Figure 12b indicates predicted s values where m_{brine}(T) was assigned the constant value m_{brine}(T = −15°C).

[57] Comparison of Figures 12a and 12b shows that taking into account the temperature dependence of m_{brine} significantly enhances s for brine pockets and tubes at temperatures below −15°C and significantly decreases their s values at temperatures higher than −15°C. Because the refractive index of mirabilite and hydrohalite is generally larger than m_{brine}(T), the effect of scattering by these salts diminishes as the ice is cooled below −15°C. Because $|m_{rel} - 1|$ for gas in brine is relatively large, temperature-dependent changes in m_{brine} have negligible impact on scattering by gas bubbles. The dashed line in Figure 11 indicates that without the full representation of m_{brine}(T), our model would significantly over-predict the temperature dependence of s(T) for the laboratory sample. While it is likely that s for T < −22.9°C is more sensitive to the effective size of precipitated crystals than to the exact representation of m_{brine}(T) at the highest temperatures, the effect of m_{brine}(T) is to dramatically reduce the efficacy of scattering by brine

inclusions. This results in a gradual lessening of importance of the microstructure with increased temperature, and a gradual increasing of importance of m_{brine}(T) with increased temperature.

[58] While a model formulated strictly on the temperature-dependent changes in m_{brine}(T) does a reasonable job of predicting the temperature-dependence of structural-optical properties in sea ice, and would be attractive for its wide applicability to all types of sea ice, it specifically fails to account for the total magnitude of *s*. The role of ice salinity in determining the magnitude of *s* will be addressed next.

7.2. Role of Ice Salinity

[59] Since the bulk ice salinity dictates brine volume and the total mass of precipitated salt, the overall magnitude of the scattering is expected to depend strongly on salinity. We first present application of the model to a high salinity ice sample, and then discuss the sensitivity of the model to ice salinity.

[60] Independent optical data that can be used for testing the structural-optical model were collected by *Erickson* [2002]. These data were taken from 10-cm thick samples of high salinity, laboratory-grown sea ice. The ice was grown at −20°C with average salinity 15 ppt and a bulk density of 0.90 Mg m^{-3}. Although detailed structural data were not collected, apparent optical properties were measured and the MCM was used to derive *s*(T) in the same manner as was done for Figure 4. Figure 13 shows the observations (points) for this high salinity sample. Note that *s* values for the 15 ppt sample are ∼3 times larger than *s* values for the 4.7 ppt sample.

[61] The structural-optical model was run for the high salinity sample. The brine inclusion size distribution was extended to include tubes as large as $l = 45$ mm to account for the additional brine volume. While larger brine tubes were added to the distribution, the number density of smaller brine inclusions was the same as used to model the 4.7 ppt ice. Scattering by precipitated salt crystals was adjusted for the increased salinity by increasing the crystal number density. Effective crystal sizes inferred from the low salinity case (10 μm for mirabilite and 4.5 μm for hydrohalite) were used, assuming that salinity does not affect crystal size, although this has not been specifically studied. The active gas bubble size and number parameterizations adopted for the low salinity case (section 6) were also used for this ice. As with the lower salinity case, this parameterization produced only 30% of the total gas volume necessary to explain the observed bulk density. Also, as with the lower salinity case, the bulk density would have had to been larger (0.923 Mg m^{-3}) to be fully consistent with our bubble parameterization.

[62] To achieve agreement with the optical observations, the percentage of drained tubes had to be increased from 3% to 14% for the high salinity case. This is reasonable given that the brine volume of the high salinity sample was three times larger than the lower salinity case, likely leading to significantly larger brine drainage.

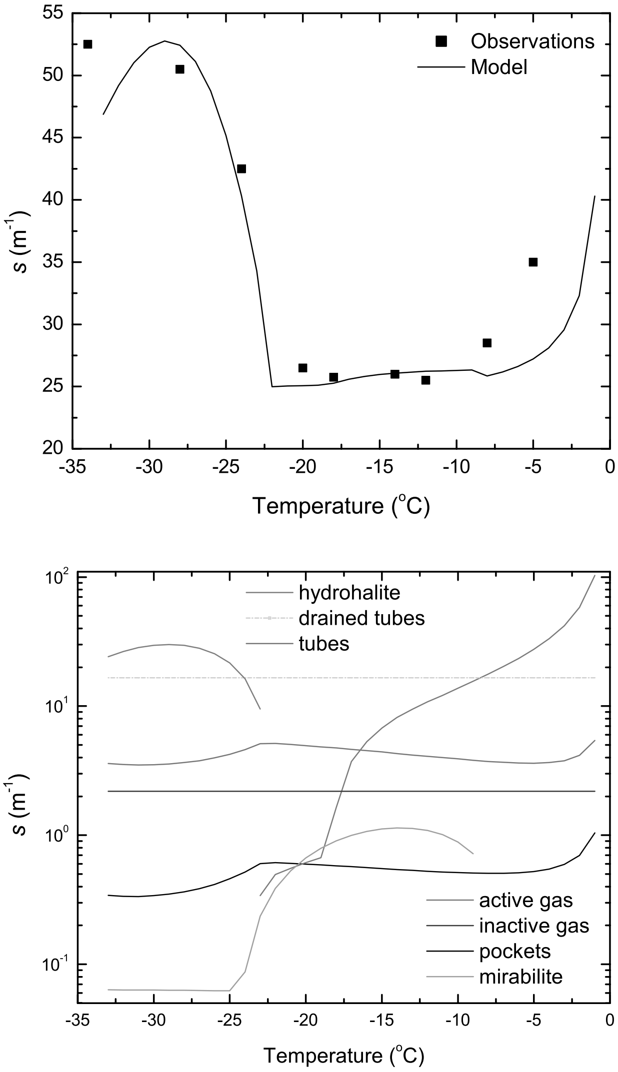

Figure 13. Observations and model predictions for a high salinity sea ice sample, (a) comparison between *s* derived from observations and predicted with model, (b) model-predicted similarity parameters for each constituent. See color version of this figure at back of this issue.

[63] The solid line in Figure 13a shows model predicted *s*(T) for the high salinity sample. The model explained observed scattering in the mirabilite regime and at −28°C in the hydrohalite regime. As in the lower salinity case, hydrohalite crystals dominate scattering at low temperatures. Attenuation by scattering in this temperature regime depends on the size, number, and total mass of crystals, rather than their exact arrangement in the ice or the size and shape of the host brine inclusions. The optical properties of cold ice are thus controlled primarily by the precipitation patterns of the hydrohalite crystals, their dielectric properties, and the bulk ice salinity. However, scattering was under-predicted at −34°C, suggesting that the assumption of constant crystal size may need to be modified. The high salinity ice had greatly increased scattering above −8°C which the model was unable to predict, even when gas bubble escape and brine inclusion merging were disabled. Since brine was observed to leak out of the sample at high temperatures, it is likely this increased scattering was caused by additional brine tube drainage.

[64] In the mirabilite regime, the results suggest that the balance between increased scattering by brine and gas inclusions with warming and decreased scattering by mirabilite crystals still holds, despite the enhanced salinity.

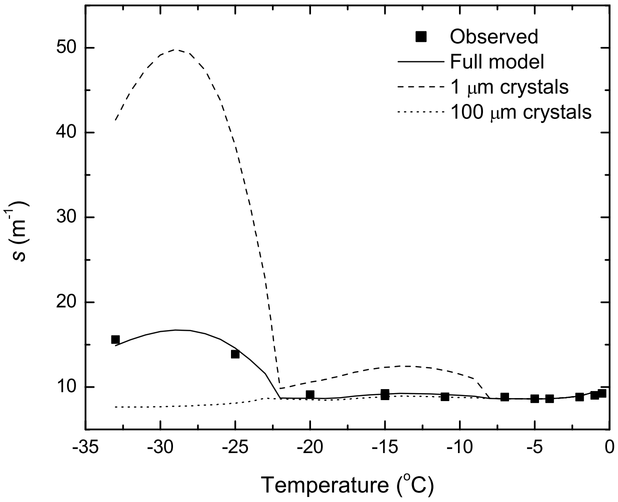

Figure 14. Effects of precipitated crystal size on the temperature dependence of the similarity parameter.

Again, it appears this result is fairly insensitive to the details of the microstructure, so that scattering in a wide variety of other sea ice types is also likely to exhibit weak temperature dependence in the mirabilite regime.

[65] The bulk salinity appears to affect the magnitude of total scattering, while the temperature dependence is more dependent on $m_{\mathrm{brine}}(\mathrm{T})$ and, possibly, on the microstructure, as will be explored in the following section.

7.3. Role of Microstructure

[66] A number of model simulations were carried out to examine how changes in salt crystal, gas bubble, and brine inclusion distributions affect structural-optical relationships in sea ice.

7.3.1. Salt Crystal Size and Number

[67] Effective crystal sizes in the full model were assumed to be 10 μm for mirabilite, and 4.5 μm for hydrohalite, both independent of temperature. The crystal number is constrained by the total precipitable mass, as determined by freezing-equilibrium. Figure 14 shows the sensitivity of $s(\mathrm{T})$ to crystal size. Simulations were run with effective crystal size increased to 100 μm (dotted line) and decreased to 1 μm (dashed line). Increased crystal size had little impact on $s(\mathrm{T})$ for mirabilite since scattering by 10 μm crystals was already relatively small, whereas increasing the hydrohalite size from 4.5 μm to 10 μm dramatically decreased scattering at the lowest temperatures. Decreasing both effective crystal sizes to 1 μm significantly enhanced σ for each type of crystal. However, despite significant increases in σ, effects of $m_{\mathrm{brine}}(\mathrm{T})$ still reduced attenuation by scattering for mirabilite at temperatures below -15°C and for hydrohalite below about -29°C.

[68] There may likely be other factors that affect scattering by precipitated salt crystals. Perhaps the most outstanding uncertainty is the prediction of single scattering phase functions for individual crystals. The calculations of phase functions for precipitated salt crystals were done using Mie theory, modeling the crystals as equivalent spheres, ignoring effects of the faceted crystal geometry. Both crystals form in the monoclinic system and have planar faces and sharp edges. We would expect the explicit treatment of single scattering by such crystals to produce considerably smaller values of g, commensurate with smaller inferred values of σ and larger inferred effective size, but we are not aware of single scattering calculations specifically for mirabilite and hydrohalite crystals in brine. There is also some evidence that ice crystals may cocrystallize with hydrohalite within the inclusions, further complicating the characterization of scattering at low temperatures.

7.3.2. Gas Bubble Size and Number

[69] The sensitivity to active gas bubbles was investigated by first doubling their fractional volume in brine inclusions, then by doubling the number of brine inclusions containing bubbles. Both tests doubled the total active gas volume. Doubling the volume of individual bubbles (Figure 15, dashed line) produced only slightly enhanced s values in the mirabilite regime. There was also little effect in the warm regime because bubbles with radius $r > 0.16$ mm were still assumed to escape from the ice. Doubling the number of active gas bubbles (Figure 14, dotted line), however, strongly increased scattering. Doubling the number means that 80% of all brine tubes would contain bubbles at -15°C, contrary to the microstructural observations of 40%. The optical properties are more sensitive to the number simply because σ doubles when N doubles, but when the volume of individual inclusions is doubled, σ increases by only 1.59. At this point, the behavior and nucleation patterns of gas bubbles within brine inclusions remain poorly understood but are clearly important.

7.3.3. Distribution of Brine

[70] In this study, scatterers have been treated as being uniformly distributed and randomly oriented, a condition for the application of equivalent spheres. There is, however, ample evidence that the microstructure of first-year sea ice is generally oriented, such that brine tubes and strings of brine pockets are generally aligned or stacked vertically [e.g., *Cole and Shapiro*, 1998; *Light et al.*, 2003a]. Long, straight-walled tubes with perfect vertical alignment should predominantly scatter light by azimuthal redistribution, which would not modify the irradiance attenuation. The

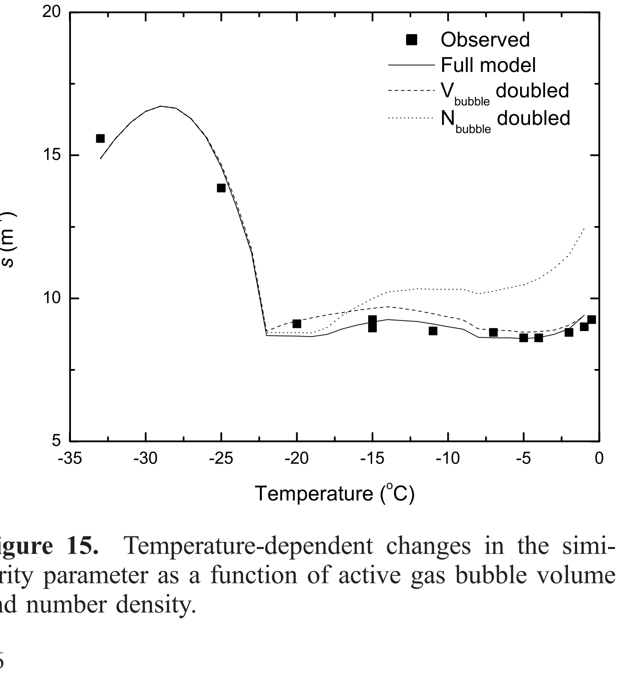

Figure 15. Temperature-dependent changes in the similarity parameter as a function of active gas bubble volume and number density.

Table 1. Representative Values of s, κ, σ, and g[a]

Temperature Regime	s, m^{-1}	κ	σ, m^{-1}	g
Low T: T < −23°C	11.6–16.7	$\kappa_{ice}(\lambda)$	1002–3060	0.988–0.995
Medium T: −23°C < T < −8°C	8.7–9.3	$\kappa_{ice}(\lambda)$	401–474	0.978–0.982
High T: T > −8°C	8.6–9.4	$\kappa_{ice}(\lambda)$	341–448	0.975–0.979

[a] Values are applicable to a sample of 4.7 ppt first-year, interior sea ice, observed under laboratory conditions. The $\kappa_{ice}(\lambda)$ indicates the spectrally-dependent absorption coefficient for pure ice.

structural alignment thus potentially impacts treatment of the IOPs for the microstructure.

[71] Furthermore, it is likely that much of the in situ laboratory brine drainage may not ordinarily occur within pack ice. Eliminating the scattering contribution from drained tubes would reduce $s(-15°\text{C})$ from 9.2 to 6.6 m^{-1}. Drained tubes do not respond to changes in temperature, and thus do not significantly impact the temperature response of $s(\text{T})$. Gas bubble escape was also a key parameterization in developing the full model. Clearly, if gas bubbles fail to escape from the ice, particularly from the interior, the model shows that $s(\text{T})$ would increase rapidly at high temperatures. This could have important implications for the optical properties of melting sea ice, but not enough is currently known about gas bubbles in ice to properly quantify under what conditions they would escape or be retained.

8. Conclusions

[72] The structural-optical model developed in this study is a useful tool for predicting inherent optical properties of first-year sea ice directly from information about ice temperature, bulk salinity, and the distribution of brine, gas, and salt inclusions. Three temperature regimes were identified, each exhibiting a distinct relationship between the ice microstructure and its inherent optical properties. In general, sea ice exhibits strong forward scattering, with bulk g values ranging between 0.86 for fresh bubbly ice and 0.98–0.99 for first-year interior ice. Table 1 gives a summary of suggested values of s, κ, σ, and g for each of the three temperature regimes for the model developed in this work as applied to a sample of 4.7 ppt first-year interior sea ice as observed under laboratory conditions (see Figure 11).

[73] Since the temperature, salinity, and brine and gas distributions ultimately control the chemical, dielectric, and microstructural properties of sea ice, ties between the physical and optical properties of the ice are inextricably linked to freezing equilibrium. Freezing equilibrium impacts the optical properties of sea ice in two fundamental ways. Scattering coefficients for inclusions of brine, gas, and salt respond to changes in constituent volumes determined by freezing equilibrium. As brine inclusions and active gas bubbles grow and shrink and salt crystals precipitate and dissolve, scattering coefficients reflect changes in the total cross-sectional area of each population. Also, scattering phase functions for brine in ice, gas in brine, and salt crystals in brine respond to changes in the dielectric properties of brine, as dictated by freezing equilibrium. In addition to these important temperature-dependent processes, inactive gas bubbles contributed significant scattering to the laboratory sample. Little is known about the distribution of inactive gas in sea ice, but it is clearly an important component of the total scattering, it least in the ice we sampled.

[74] The AOPs of sea ice are surprisingly independent of the strong temperature-dependent changes that occur in the microstructure of warm ice. This behavior is likely due to the strong scattering by inactive gas, but is also attributable to a balance between increasing scattering coefficient and increasing g as the brine becomes more dilute and its refractive index decreases. There is an analgous balance between increasing brine inclusion size and decreasing mirabilite crystal number density which also acts to minimize the temperature-dependence of the AOPs at moderate temperatures (−23°C < T < −8°C). At lower temperatures, poorly understood details of the hydrohalite precipitation control the AOPs, but these conditions are of little practical importance. Most cases of geophysical interest occur at T > −23°C where, because of the various balances, it should be possible to develop relatively simple AOP parameterizations suitable for use in large-scale models.

[75] It should be noted, however, that the results reported here are based on data collected in the laboratory from interior first-year ice. While the magnitude of in situ optical properties are likely to be different than the laboratory values, the temperature dependence should be similar, except at very high temperatures where the ice may exhibit significant differences in brine drainage (i.e., in the volume of inactive gas) and the loss of active bubbles. Likewise, little is known about the detailed microstructure of multiyear ice and the degree to which the structural-optical model can predict AOPs in such ice is uncertain. The extent of our quantitative understanding of the structural-optical properties and processes that occur in sea ice is likely to increase as additional field observations are focused on the topic and more effort committed to modeling these processes.

[76] **Acknowledgments.** This research was supported by the Office of Naval Research, Arctic Program under grants N00014-90-J-1075, N00014-94-1-0791, N00014-97-1-0765, and N00014-03-1-0120, and the National Science Foundation, Office of Polar Programs under grant OPP-0084271.

References

Abramowitz, M., and I. A. Stegun (Eds.) (1965), *Handbook of Mathematical Functions With Formulas, Graphs, and Mathematical Tables*, 1046 pp., Dover, Mineola, N. Y.

Chernigovskiy, N. T. (1966), Radiational properties of the central Arctic ice coat, 1963, Soviet data on the Arctic heat budget and its climatic influence, translated by J. O. Fletcher, B. Keller, and S. M. Olenicoff, *RM-5003-PR*, pp. 151–173, Rand Corp., Santa Monica, Calif.

Cole, D. M., and L. H. Shapiro (1998), Observations of brine drainage networks and microstructure of first-year sea ice, *J. Geophys. Res.*, *103*, 21,739–21,750.

Cox, G. F. N., and W. F. Weeks (1983), Equations for determining the gas and brine volumes in sea-ice samples, *J. Glaciol.*, *29*, 306–316.

Ebert, E. E., and J. A. Curry (1993), An intermediate one-dimensional thermodynamic sea ice model for investigating ice-atmosphere interactions, *J. Geophys. Res.*, *98*, 10,085–10,109.

Erickson, D. D. (2002), The optical properties of sea ice: Temperature, salinity, and wavelength dependence, M.S. thesis, Univ. of Wash., Seattle, Wash.

Grenfell, T. C. (1983), A theoretical model of the optical properties of sea ice in the visible and near infrared, *J. Geophys. Res.*, *88*, 9723–9735.

Grenfell, T. C. (1991), A radiative transfer model for sea ice with vertical structure variations, *J. Geophys. Res.*, *96*, 16,991–17,001.

Grenfell, T. C., and G. A. Maykut (1977), The optical properties of ice and snow in the Arctic Basin, *J. Glaciol.*, *18*, 445–463.

Grenfell, T. C., and D. K. Perovich (1984), Spectral albedos of sea ice and incident solar irradiance in the southern Beaufort Sea, *J. Geophys. Res.*, *89*, 3573–3580.

Grenfell, T. C., and S. G. Warren (1999), Representation of a non-spherical ice particle by a collection of independent spheres for scattering and absorption of radiation, *J. Geophys. Res.*, *104*, 31,697–31,709.

Henyey, L. G., and J. L. Greenstein (1941), Diffuse radiation in the galaxy, *Astrophys. J.*, *93*, 70–83.

Holland, M. M., J. L. Schramm, and J. A. Curry (1997), Thermodynamic feedback processes in a single-column sea-ice-ocean model, *Ann. Glaciol.*, *25*, 327–332.

Jin, Z., K. Stamnes, W. F. Weeks, and S. C. Tsay (1994), The effect of sea ice on the solar energy budget in the atmosphere-sea ice-ocean system: A model study, *J. Geophys. Res.*, *99*, 25,281–25,294.

Langleben, M. P. (1969), Albedo and degree of puddling of a melting cover of sea ice, *J. Glaciol.*, *8*, 407–412.

Langleben, M. P. (1971), Albedo of melting sea ice in the southern Beaufort Sea, *J. Glaciol.*, *10*, 101–104.

Light, B. (1995), A structural-optical model of cold sea ice, M.S. thesis, Univ. of Wash., Seattle, Wash.

Light, B., G. A. Maykut, and T. C. Grenfell (2003a), Effects of temperature on the microstructure of first-year Arctic sea ice, *J. Geophys. Res.*, *108*(C2), 3051, doi:10.1029/2001JC000887.

Light, B., G. A. Maykut, and T. C. Grenfell (2003b), A two-dimensional Monte Carlo model of radiative transfer in sea ice, *J. Geophys. Res.*, *108*(C7), 3219, doi:10.1029/2002JC001513.

Maykut, G. A., and T. C. Grenfell (1975), The spectral distribution of light beneath first-year sea ice in the Arctic Ocean, *Limnol. Oceanogr.*, *20*, 554–563.

Maykut, G. A., and B. Light (1995), Refractive-index measurements in freezing sea-ice and sodium chloride brines, *Appl. Opt.*, *34*, 950–961.

Maykut, G. A., and N. Untersteiner (1971), Some results from a time-dependent, thermodynamic model of sea ice, *J. Geophys. Res.*, *76*, 1550–1575.

Mobley, C. D., G. F. Cota, T. C. Grenfell, R. A. Maffione, W. S. Pegau, and D. K. Perovich (1998), Modeling light propagation in sea ice, *IEEE Trans. Geosci. Remote Sens.*, *36*, 1743–1749.

Mobley, C. D., L. K. Sundman, and E. Boss (2002), Phase function effects on oceanic light fields, *Appl. Opt.*, *41*, 1035–1050.

Moritz, R. E. and D. K. Perovich (1996), *SHEBA: Science Plan*, 60 pp., ARCSS OAII Manage. Off., Polar Sci. Cent., Univ. of Wash., Seattle, Wash.

Nelson, K. H., and T. G. Thompson (1954), Deposition of salts from sea water by frigid concentration, *J. Mar. Res.*, *13*, 166–182.

Pegau, W. S., and J. R. V. Zaneveld (2000), Field measurements of in-ice radiance, *Cold Reg. Sci. Tech.*, *31*, 33–46.

Perovich, D. K. (1990), Theoretical estimates of light reflection and transmission by spatially complex and temporally varying sea ice covers, *J. Geophys. Res.*, *95*, 9557–9567.

Perovich, D. K. (1994), Light reflection from sea ice during the onset of melt, *J. Geophys. Res.*, *99*, 3351–3359.

Perovich, D. K., et al. (1998a), Field observations of the electromagnetic properties of first-year sea ice, *IEEE Trans. Geosci. Remote. Sens.*, *36*, 1705–1715.

Perovich, D. K., C. S. Roesler, and W. S. Pegau (1998b), Variability in Arctic sea ice optical properties, *J. Geophys. Res.*, *103*, 1193–1208.

Perovich, D. K., T. C. Grenfell, B. Light, and P. V. Hobbs (2002), Seasonal evolution of the albdo of multiyear Arctic sea ice, *J. Geophys. Res.*, *107*(C10), 8044, doi:10.1029/2000JC000438.

Pounder, E. R. (1965), *The Physics of Ice*, 151 pp., Pergamon, New York.

Richardson, C. (1976), Phase relationships in sea ice as a function of temperature, *J. Glaciol.*, *17*, 507–519.

Untersteiner, N. (1961), On the mass and heat budget of arctic sea ice, *Arch. Meteorol. Geophys. Bioklimatol., Ser. A*, *12*, 151–182.

van de Hulst, H. C. (1980), *Multiple Light Scattering Tables, Formulas, and Applications*, vols. 1 and 2, 739 pp., Academic, San Diego, Calif.

T. C. Grenfell and G. A. Maykut, Department of Atmospheric Sciences, University of Washington, Seattle, WA 98195, USA.

B. Light, Applied Physics Laboratory, Polar Science Center, University of Washington, Seattle, WA 98105, USA. (bonnie@apl.washington.edu)

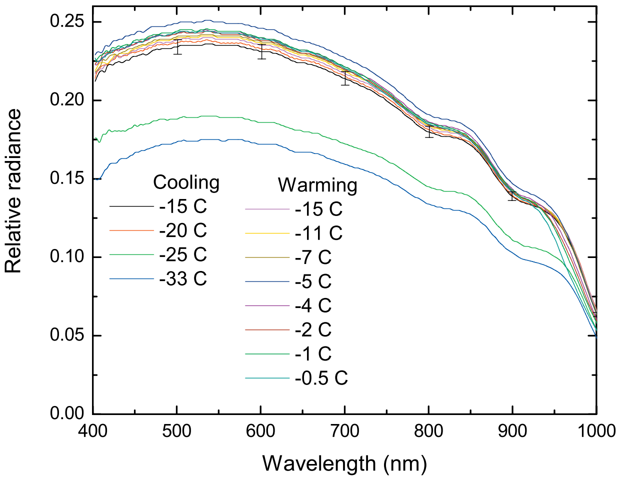

Figure 3. Temperature-dependent changes in spectral radiance transmitted at 30° from nadir. Radiances were measured through the glass plate used to support the sample, then normalized by the incident irradiance.

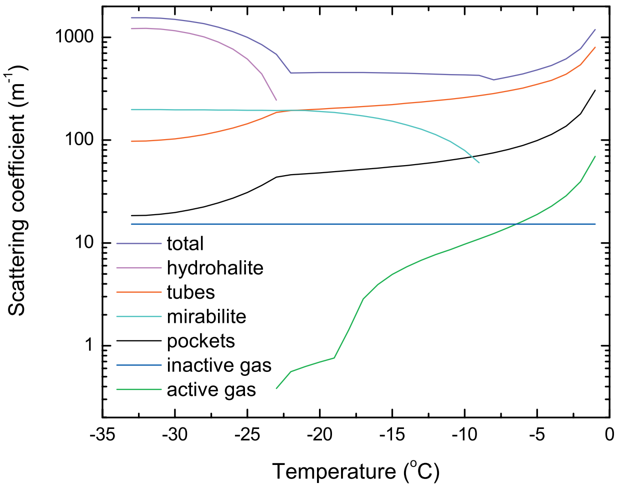

Figure 5. Temperature-dependent scattering coefficients for various types of scatterers in sea ice as predicted by the structural-optical model.

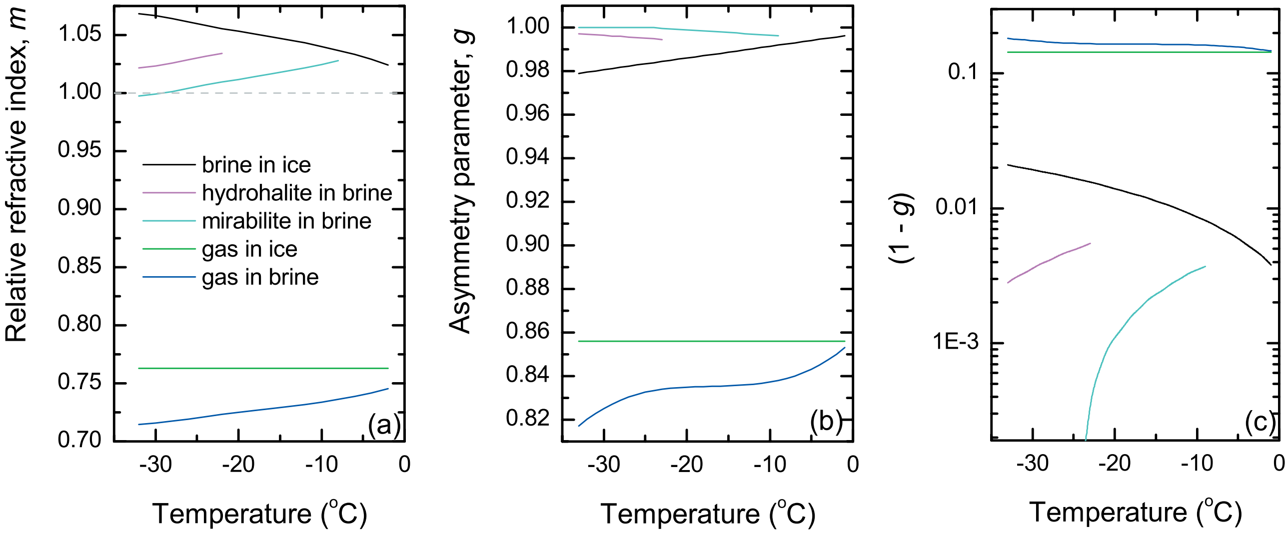

Figure 7. Temperature dependence of (a) relative refractive index, (b) asymmetry parameter, g, and (c) $[1 - g]$ for inclusions of brine in ice, gas in ice, gas in brine, mirabilite in brine, and hydrohalite in brine. Asymmetry parameters were calculated using equivalent spheres and Mie theory.

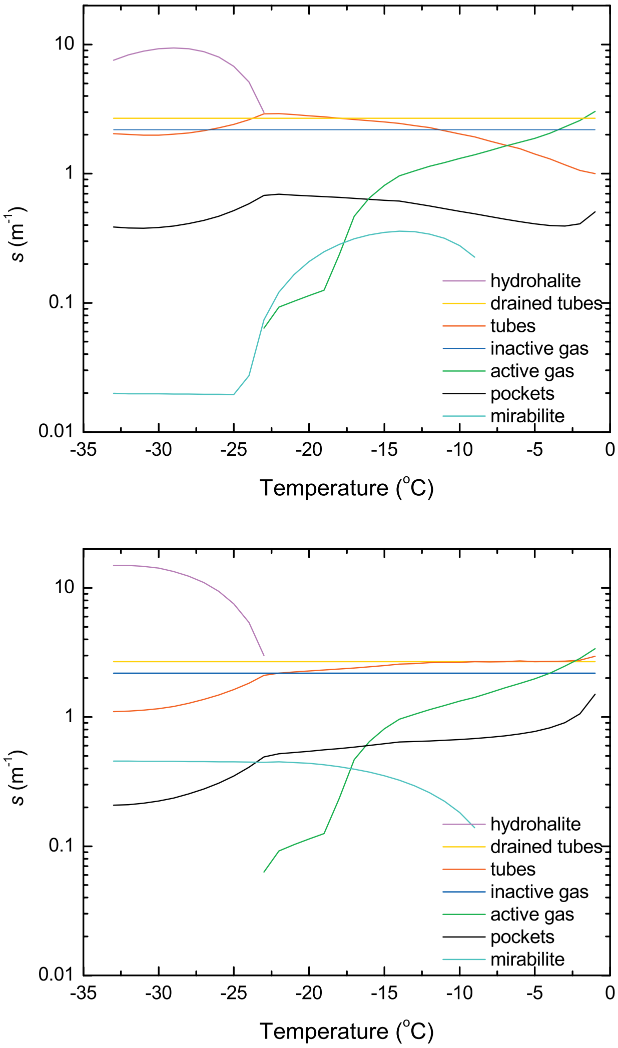

Figure 12. Temperature-dependent partial similarity parameters for each constituent in the full structural-optical model using (a) $m_{\mathrm{brine}}(\mathrm{T})$ and (b) $m_{\mathrm{brine}}(\mathrm{T} = -15°\mathrm{C})$.

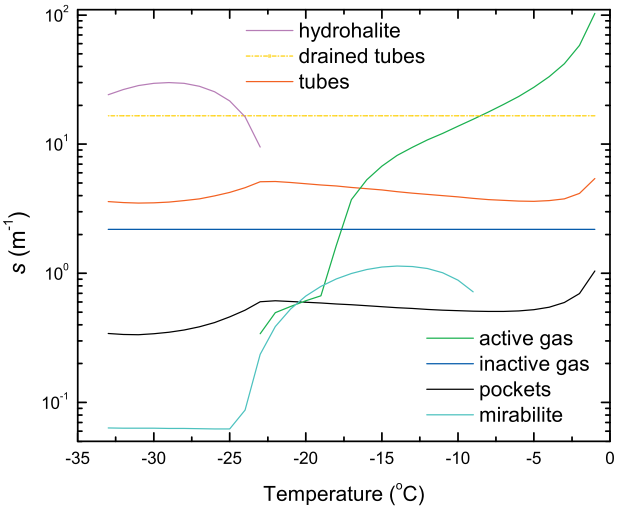

Figure 13. Observations and model predictions for a high salinity sea ice sample, (a) comparison between *s* derived from observations and predicted with model, (b) model-predicted similarity parameters for each constituent.